International Journal of Thermal Sciences 171 (2022) 107245

Contents lists available at ScienceDirect

International Journal of Thermal Sciences

journal homepage: www.elsevier.com/locate/ijts

Predicting the conductive heat transfer through evacuated perlite based vacuum insulation panels

Sankarshan Verma, Harjit Singh *

Institute of Energy Futures, College of Engineering, Design and Physical Sciences, Brunel University London, Uxbridge, UB8 3PH, UK

ARTICLE INFO

Keywords:
Perlite
Porous insulation
Vacuum insulation
COMSOL Multiphysics
Conductive heat transfer

ABSTRACT

The core material contributes ≥40% of the total cost of a fumed silica based vacuum insulation panel (VIP). Expanded perlites, which come at approximately one-tenth of the current price of fumed silica, have been identified as potential core material candidates. Though, the characteristic vacuum insulation properties i.e. evacuated thermal conductivity and half pressure value of expanded perlites are not suitable for most applications, these can be improved by altering their structural properties like particle size, pore size, porosity etc. during manufacture. The knowledge of the relationship between structural properties and the thermal conductivity of perlite is key to develop improved thermal performance VIPs.

In the present work, it has been found that the thermal conductivity of the perlite cores lies between the thermal conductivities of two regular packing orders – simple cubic packing and the hexagonal close packing. Owing to the complex geometries involved, the thermal conductivity of particle beds arranged in these two packing structures was numerically calculated using finite element method. The dependence of the thermal conductivity on five parameters (particle size, intra-particle pore size, porosity, internal gas pressure and contact ratio) was observed and correlated with existing studies in literature. The model was also validated by experiments performed on expanded perlite. The developed framework can be employed to produce bespoke perlites for most cost-effective thermal insulation systems.

1. Introduction

The core material contributes ≥40% of the total cost of a fumed silica based vacuum insulation panel (VIP) [1,2], consequently research into potentially reduced cost core materials have been increasingly reported recently [3–9]. Expanded perlites, which come at approximately one-tenth of the current price of fumed silica, have been identified as potential core material candidates. Apart from being a VIP core, evacuated perlites in their loose state can also be directly used as insulation in various situations such as thermal storage tanks or cold storage boxes.

Although the chemical composition of both perlite and fumed silica is very similar, >90% being SiO_2, and both belong to the category of powder insulants, yet there is a stark difference between their thermal conductivities. This is caused by their dissimilar particle arrangement order (geometric structure) and the structural properties such as particle size, pore size and porosity. The authors of this paper have recently described several parameters that affect the thermal conductivity of a VIP core [10]; see Fig. 1.

Interestingly, most of these parameters can be controlled either during perlite manufacturing (particle/pore size, porosity) or insulation manufacturing (pressure, density) process. Knowledge of the quantitative contribution of these parameters towards the thermal conductivity of evacuated perlite is the key to develop high-performance cost-effective VIPs.

The aim of the present study was to develop a framework, based upon the physics of heat transfer and particles' interaction at the microscopic level, which takes as an input the set of values of various affecting parameters identified above and returns the value of predicted thermal conductivity.

So far, a very limited number of studies have reported the development of such a theoretical framework to predict the thermal conductivity of perlites. However, such frameworks have been extensively reported for nano-porous insulants like aerogel/fumed silica which could provide a starting point. Two types of models have been predominantly used to develop such frameworks, i) Decoupled model, ii) Energy balance model [11].

The decoupled model assumes that the total heat travelling through the insulant by three different modes, solid-solid conduction, gas conduction in open pores and radiation, are independent from each other.

* Corresponding author.
E-mail address: harjit.singh@brunel.ac.uk (H. Singh).

https://doi.org/10.1016/j.ijthermalsci.2021.107245
Received 29 June 2021; Received in revised form 20 August 2021; Accepted 23 August 2021
Available online 3 September 2021

Nomenclature

a	Contact diameter
D	Particle diameter
D_p	Diameter of pore
D_{pc}	Diameter of crosswise pore
d_g	Molecular size of the gas
e	Extinction coefficient
f	function to calculate thermal conductivity (Fourier's law)
k_{total}	Total thermal conductivity (10^{-3} $Wm^{-1}K^{-1}$)
k_s	Solid thermal conductivity
k_g	Gaseous thermal conductivity
k_r	Radiative thermal conductivity
k_{coup}	Coupling conductivity
k_g^0	Thermal conductivity of free air
k_B	Boltzmann constant
k_{gr}	Thermal conductivity of grain
k_T	Thermal conductivity of base material
k_c	Conductive thermal conductivity
$k_{VIP,\ measured}$	total measured thermal conductivity of a VIP
l_g	Mean free path length of air
m_{total}	Bulk porosity of powder
m	Porosity of a powder particle
n	real part of refractive index
p	Gas pressure
$p_{1/2}$	Half pressure of a VIP
$\dot{Q}$	Rate of heat transfer
S	total surface area of the pore
T	Temperature

Greek symbols

β	Constant used in gaseous conductivity calculation
ν	Ratio of k_T and k_g
ρ	density
ρ_s	skeletal density
σ	Stefan-Boltzmann constant

Abbreviations

VIP	Vacuum Insulation Panel
SEM	Scanning Electron Microscopy
MIP	Mercury Intrusion Porosimetry
NuSC	Numerical Simple Cubic model
NuHex	Numerical Hexagonal model

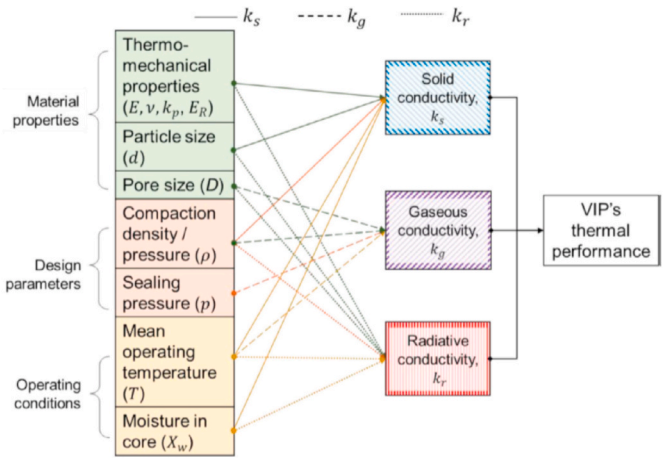

Fig. 1. Various factors affecting the thermal conductivity of a VIP [10].

The total thermal conductivity is thus, the sum of solid conductivity, gaseous conductivity and radiative conductivity (equation (1)), each of which could be calculated by either a set of equations involving material properties (pore size, particle size, extinction coefficient) and design parameters (pressure, density) or experimental best-fitting techniques [3,12–14].

$$k_{total} = k_s + k_g + k_r \tag{1}$$

where k_s is the solid conductivity, k_g the gaseous conductivity and k_r the radiative conductivity of the insulant.

The decoupled model as described in equation (1) doesn't account for the heat travelling from solid to gas or vice versa. To balance this missing effect, a term, called coupling conductivity (k_{coup}), is generally added [15].

The major drawback of the decoupled model is that it requires a separate computation of solid-gas coupling, which is not well understood, but has a significant effect in spherical particle porous insulation materials like perlite at pressures higher than 10 mbar. Coupling conductivity for expanded perlite is likely to be 20–30 $mWm^{-1}K^{-1}$, approximately 30% of the total thermal conductivity at atmospheric pressures [16]. Beikircher et al. [17] calculated the coupling conductivity to be 3.2 $mWm^{-1}K^{-1}$ at 10 mbar and 15 $mWm^{-1}K^{-1}$ at atmospheric pressure. Though Beikircher et al. [17] developed a set of equations to calculate the coupling conductivity, the parameters in the equations were derived using rather simple best-fitting techniques. This made their model dependent on experimental data which limited its capability to predict for materials outside their study. Theoretical model to compute coupling conductivity in aerogel have been developed but the model assumptions, based on the microstructure of aerogel, don't hold for perlite, which has a different microstructure [15,18]. Alam et al. [19] measured the value of coupling conductivity for perlite-fumed silica composites at atmospheric pressure to be around 12 $mWm^{-1}K^{-1}$. This clearly indicates that one cannot neglect coupling effect whilst developing a predictive framework for perlites and hence a decoupled model might not be the best method to solve for it.

The second type of predominantly used model is the energy balance model in which the microstructure of insulant is approximated as a regular geometric structure composed of repeating unit cells. The thermal conductivity of the insulant, being an intrinsic property, must be same as the thermal conductivity of the smallest unit cell. Heat travelling from one end of the unit cell to the other through conduction (solid and gaseous) is calculated and transformed to the thermal conductivity using Fourier's law. Heat transfer through radiation is simply superimposed to the heat transfer through conduction, and convection in insulant pores is neglected, due to their small size (<2 mm).

Zeng et al. [20] derived the relationship between thermal conductivity and structural properties of aerogel assuming aerogel's geometric structure to be formed of repeated unit cells of any of the three regular structures - arrays of square rods, cylindrical rods and contacting spheres. A similar method was employed by Lu et al. [21] and Wei et al. [22,23] and to calculate the thermal conductivity of aerogel and its composites, assuming different types of unit cells. However, this method suffers from the following drawbacks:

i. The heat transfer is considered to be one dimensional, which means the solid-solid heat flow at the solid-gas boundary is not considered. This may become a significant source of deviation when the intra-particle porosity of insulant is low.

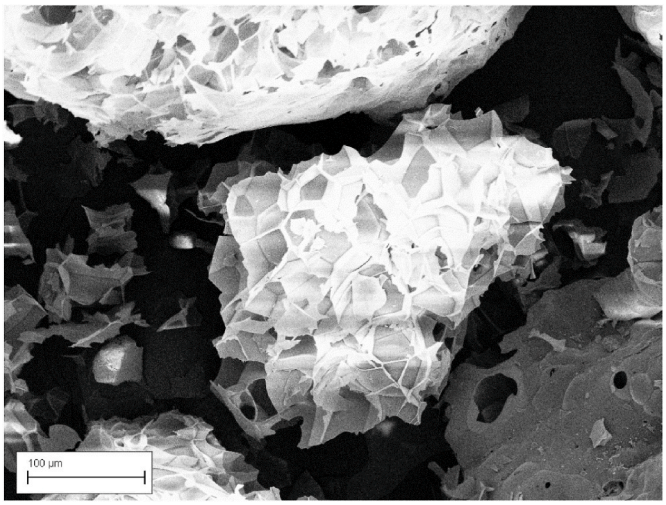

Fig. 2. SEM image of an expanded perlite particle.

ii. It can only be used to resolve unit cells of simple geometries, like cubic and intersecting rods but not complex geometries like hexagonal unit cell.
iii. It cannot provide detailed information of temperature and heat flux fields in the insulant.

These drawbacks could be solved if the heat flow through various modes is calculated numerically instead, as done by Bi et al. [24] to predict the thermal conductivity of aerogel. Unfortunately, no such study exists for expanded perlites. Further, it is noteworthy that both aerogels and perlites don't have a regular structure because of their non-crystalline nature. Due to this reason, it is impossible to identify a single unit cell which represents the geometric structure of these powders. However, the thermal conductivity of the random structure (particle arrangement) of perlites could be bound by that of two regular structures.

In the present study, the authors have investigated into employing energy balance based numerical method for expanded perlite powder, which is equivalent to a bed of spherical porous particles.

This resulted into the development of a theoretical framework to predict the upper and lower bounds of conduction heat transfer of porous spherical perlite, incorporating the effects of a) particle size, b) pore size, c) porosity, d) pressure and e) contact ratio among particles (section 2.1–2.3). The model was experimentally validated through in-lab measurements on VIPs specifically developed using expanded perlites (section 3). The effect of radiative heat transfer due to VIP envelope was accounted for when calculating total thermal conductivity.

Although the present work was focused towards expanded perlites, the framework could be used to analyse the variation of thermal conductivity for any similar porous insulation with spherical particles, such as glass beads, with their material and design properties.

2. Modelling heat transfer in perlite

Heat transfer in a porous insulation occurs via conduction and radiation. The former comprises of a) solid conduction through solid matrix of the insulation and b) gaseous conduction through the gas molecules inside micro-pores. Radiation heat transfer is the heat carried by electromagnetic waves (mainly in infrared region) through the material. Conduction and radiation can be assumed as parallel phenomena for an optically thick medium, i.e. a medium in which the infrared photons cannot penetrate without multiple scattering and absorptions. In such cases, the contributions of conduction and radiation can be superimposed additively [25]. The dependence of heat transfer by conduction and radiation upon the material, design and operating parameters (Fig. 1) of the vacuum insulation can be exploited to predict the thermal conductivity, thus saving huge amounts of testing costs and time.

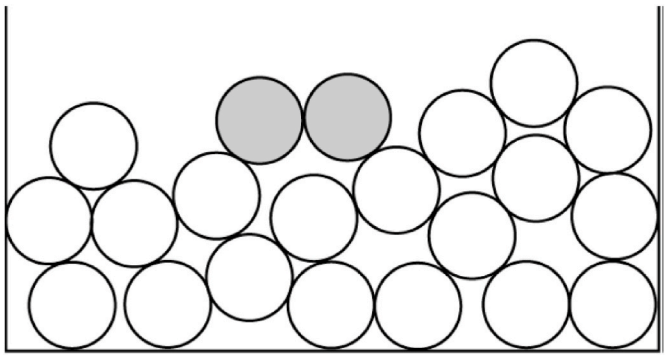

Fig. 3. A 2-D illustration of a bridge. The two shaded spheres formed a bridge while moving into a gap [31].

Expanded perlite is formed of approximately spherical shaped particles with pores on their surface, also called the intra-particle pores (Fig. 2). These pores are formed during manufacturing process when the chemically bound water (2–6%) in volcanic glass escapes as steam due to rapid heating (700–1260 °C) [26]. During this process, the volcanic glass expands about 20 times its original volume and hence the name – expanded perlite (EP). When used as an insulant, spherical EP particles pack in a random order.

All random packings of mono-sized spheres lie between two extremes i.e. random loose packing and random dense packing [27–29]. A random loose packing is identified by high amount of physical bridging and angular separation. Physical bridging occurs when two unstable spheres contact and form a stable structure (Fig. 3). This results in increase in porosity and reduction in mean coordination number [30], see Table 1. A random dense packing, which can be obtained by carefully vibrating the bed of a random loose pack, has no bridges or angular separation. Application of external pressure on a random loose pack also results in reduction of porosity and increase in the mean coordination number for elastically deformable materials [31].

Perlite, when used as a core material for VIPs, is usually pressed into boards and evacuated to low pressures [3]. The external pressure, both due to compaction of up to 0.2 MPa [12] and evacuation (up to 0.1 MPa) is expected to rearrange its elastically deformable particles into a dense random packing as detailed in Table 1.

The grain packing structure of the pressed perlite boards used as cores for VIPs must lie somewhere between normal and elastically deformed random dense packing (see Table 1), the characteristics of which are further bounded by two regular packing structures, simple cubic packing on the lower side and the hexagonal close packing on the higher side.

The thermal conductivity of this dense random pack of perlite particles, which depends majorly on the size of pores, porosity of insulant and the contacts among particles, must also be bounded by the thermal conductivity of cubic and hexagonal packings. This provides the framework of prediction of bounds of the conductive heat transfer through a dense perlite VIP core. The sections below describe the geometrical features of the two regular packings relevant to the modelling of heat transfer phenomenon.

2.1. Packing geometries

2.1.1. Modelling simple cubic packing

Simple cubic packing is the loosest possible packing for mono-sized spheres wherein each particle is in contact with six neighbouring particles with an overall pack porosity of 0.476. It is formed by repeating units consisting of two contacting hemispheres, also called simple cubic

Table 1
Characteristics of various packings of mono-sized spherical particles.

	Simple Cubic	Random loose packing	Random dense packing	Random dense packing – elastically deformed	Rhombohedral - hexagonal
Porosity	0.476	0.45–0.40 [28,32]	0.42–0.36 [28,29]	0.29 [31]	0.26
Mean coordination number	6	4.5–5.5 [30,32]	6–7 [27,33]	8 [31]	12

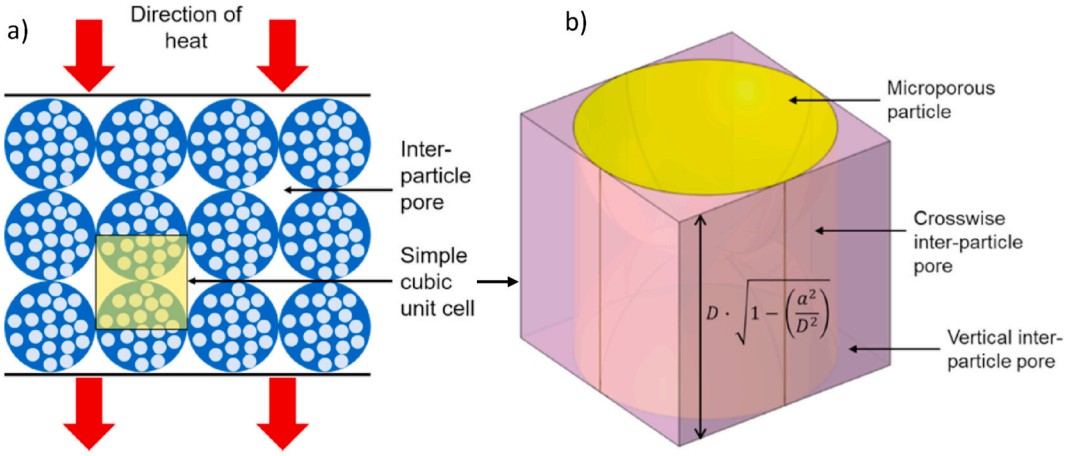

Fig. 4. A simple cubic a) packing structure and b) unit cell. The particles are shown in green colour, vertical pores in violet and crosswise pores in pink.

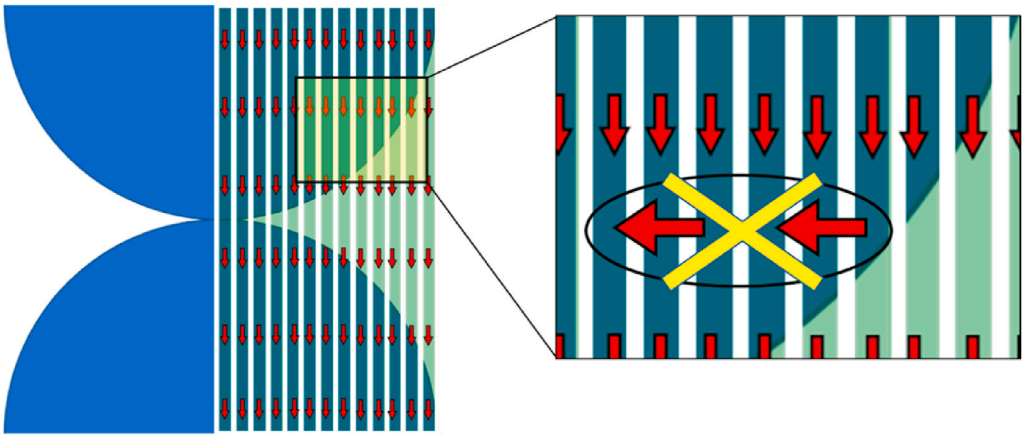

Fig. 5. Heat flow paths assumed in analytical methods. The solid-solid heat flow within the particle at solid-gas boundary is not considered in this type of solutions leading to inaccuracies.

unit cell as shown in Fig. 4. Because of its intrinsic nature, the thermal conductivity of the bulk material (bed of particles) is same as that of the unit cell. The geometry of a simple cubic cell is not complex enabling an analytical estimation of thermal conductivity using heat flowing along parallel and series paths. However, it has been found by the authors that, an analytical method employing parallel heat flow paths in concentric hollow cylindrical elements, as used by Ref. [20], can be inaccurate because it fails to consider the three-dimensional heat flow within the particle (Fig. 5.).

Porous particles arranged in simple cubic order have two types of pores; a) inter-particle pores and b) intra-particle pores, shown in Fig. 6. The pores formed by the gap between two or more neighbouring particles are termed as inter-particle pores and the porosity due to these pores is termed as inter-particle porosity. The pores present on the particle itself are intra-particle pores and the porosity of the powder due to virtue of these pores is called intra-particle porosity. The intra-particle porosity is different from on-particle porosity, m, which is the ratio of volume of intra-particle pores to the volume of particle. The total porosity of the bed, m_{total}, is the sum of inter-and intra-particle porosity. In simple cubic packing, the inter-particle pores can be of two types. First, the vertical pores, which are aligned in the direction of heat transfer when the bottom surface is warmer than the top surface, these pores run throughout the insulation thickness. Second, the cross-wise pores, the ones that are hidden due to spherical particle's circular projection.

Knudsen effect entails that heat transferred through gaseous conduction in the pores and gaseous conductivity is a function of the pore size, and is described by the Kaganer model [34] as shown in equations (2) and (3). Different characteristic pore sizes for vertical, cross-wise and intra-particle pores lead to different gaseous conductivity in these pores. The sizes of inter-particle pores can be derived from geometry. The characteristic pore size of a cross-wise pore is the average vertical

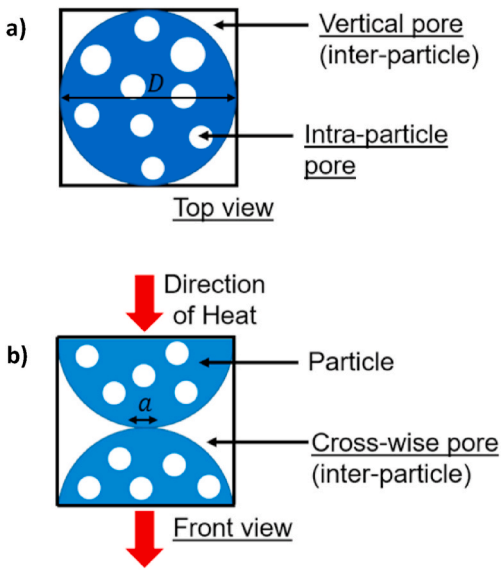

Fig. 6. Description of pores in simple cubic unit cell, a) top view, b) front view.

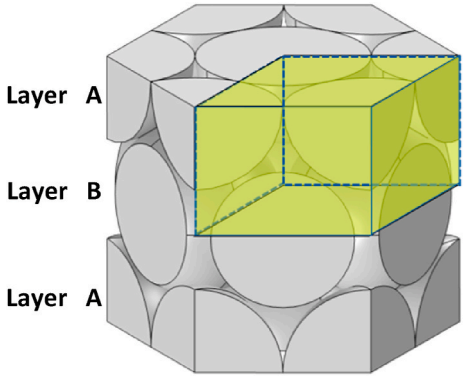

Fig. 7. Layers of particle in A-B-A configuration.

distance between the walls of two contacting particles, which can be calculated using equation (4), and of a vertical pore is the height of the unit cell. The intra-particle pore size can be calculated from SEM images.

$$k_g = \frac{k_g^0}{1 + 2\beta\frac{l_g}{D_p}} \tag{2}$$

$$l_g = \frac{k_B T}{\sqrt{2}\pi d_g^2 p} \tag{3}$$

where k_g is the gaseous conductivity of the pore, k_g^0 the conductivity of free air i.e. 25 mW m $^{-1}$K^{-1}, β the coefficient which depends on the accommodation coefficient and the adiabatic coefficient of the gas, l_g the mean free path length of gas inside pore, D_p the characteristic size of the pore, k_B the Boltzmann constant, T the temperature, d_g the molecular size of the gas and p the internal gas pressure.

The contacting particles deform when an external pressure is applied to perlite powder to form a solid core. This deformation has been represented by a contacting circular region of diameter a in the unit cell. Contact ratio, (a/D), which is defined as the ratio of diameter of circular region, a, formed as a result of deformation of two contacting particles to the diameter of the particle, D, becomes a measure of applied external pressure.

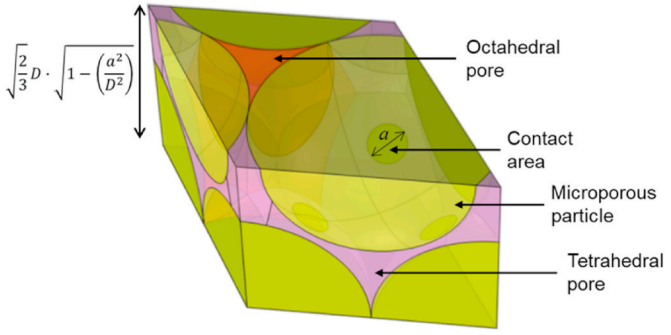

Fig. 8. A hexagonal unit cell. The particles are represented by green colour, tetrahedral pores by violet and octahedral pores by pink.

$$D_{pc} = \frac{\sum_{\theta_i=0}^{\theta_i=\sin^{-1}\left(\frac{a}{D}\right)} \left(D\left(\sqrt{1-\left(\frac{a}{D}\right)^2} - \sin\theta_i\right)\right)}{\sum_{\theta_i=0}^{\theta_i=\sin^{-1}\left(\frac{a}{D}\right)} (i)} \tag{4}$$

2.1.2. *Modelling hexagonal close packing*

Rhombohedral hexagonal packing, referred as hexagonal packing in this paper, is one of the densest packing for mono-sized spheres. Every particle in this packing is in contact with 12 neighbouring particles leading to a pack porosity (m_{total}) of 0.26. Hexagonal packing is formed by putting layers of particles in A-B-A configuration as shown in Fig. 7. The smallest non-symmetric repeating unit cell of this packing is shown in Fig. 8. This gives rise to a highly complex geometry making an analytical investigation of this packing very difficult, if not impossible.

The inter-particle pores, in the case of hexagonal packing, comprise of tetrahedral pores and octahedral pores. A tetrahedral pore is formed when a particle of layer B is in contact with three contacting particles of layer A whilst covering the pore formed by them. The size of this pore is defined as the diameter of largest sphere which can fit in, 0.225D in the case of a tetrahedral pore, where D is the particle diameter. An octahedral pore is formed when two sets of three trigonally-oriented particles in layer A and B are in close-packed contact. The size of this pore is 0.414D. The characteristic sizes of these pores are different and so is the conductivity of gas inside them; as governed by Knudsen effect.

The deformation in contacting particles in a hexagonal packing occur the same way as in simple cubic geometry. It's noteworthy there are

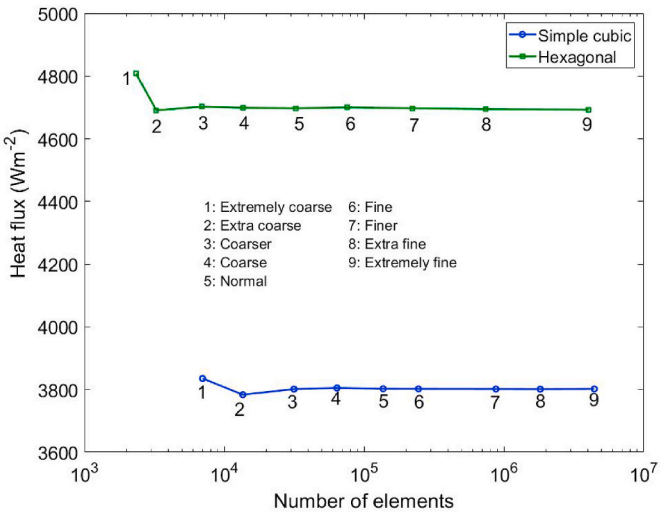

Fig. 9. Mesh independence study for two packing geometries: Simple cubic and Hexagonal.

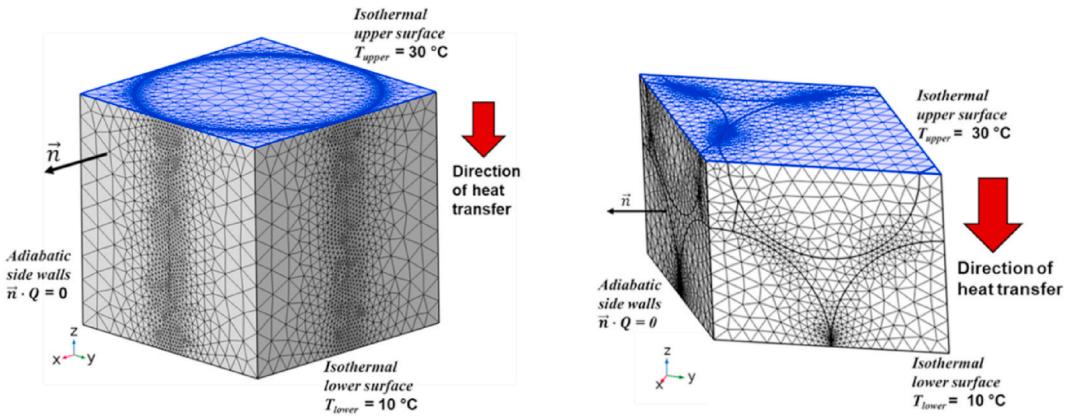

Fig. 10. A meshed geometry of a) simple cubic unit cell and b) hexagonal unit cell showing various boundary conditions.

three contact regions in the hexagonal unit cell, as compared to one in simple cubic cell, leading to a potentially higher solid conductivity.

2.2. Numerical modelling for conduction heat transfer

As mentioned in the sections above, solving heat transfer in these geometries using analytical method of series and parallel resistance networks can be either inaccurate or very difficult due to complex geometries involved. Keeping this in mind, an approximate solution was computed using finite element method, solved in COMSOL Multiphysics V.5.5. The finite element method is different from finite difference method since it solves the partial differential equations in an integral form. The finite element method has clear advantages in terms of its adaptability to complex geometries and the ease of handling discontinuous gradients of a variable [35].

2.2.1. Mesh independence and boundary conditions

A fully parametric geometry of the unit cells was developed and the solution domain was discretized using tetrahedral elements. Mesh independence studies showed that heat flux at faces became steady after 'normal' mesh size (Fig. 9). The normal mesh size in COMSOL was characterized by minimum element sizes of 2.5 μm and 3.5 μm and maximum element sizes of 20 μm and 48 μm, respectively for cubic and hexagonal geometries. The boundary conditions on the meshed geometries are shown in Fig. 10. The unit cells were subjected to a temperature difference of 20 °C between isothermally held upper and lower faces. A mean temperature of 20 °C was chosen because the thermal conductivity of the commercial VIPs is reported at this temperature. The four lateral faces of the unit cell were assumed to be adiabatic because of symmetrical nature of the regular packing structures. The initial temperature of both geometries was set at 20 °C.

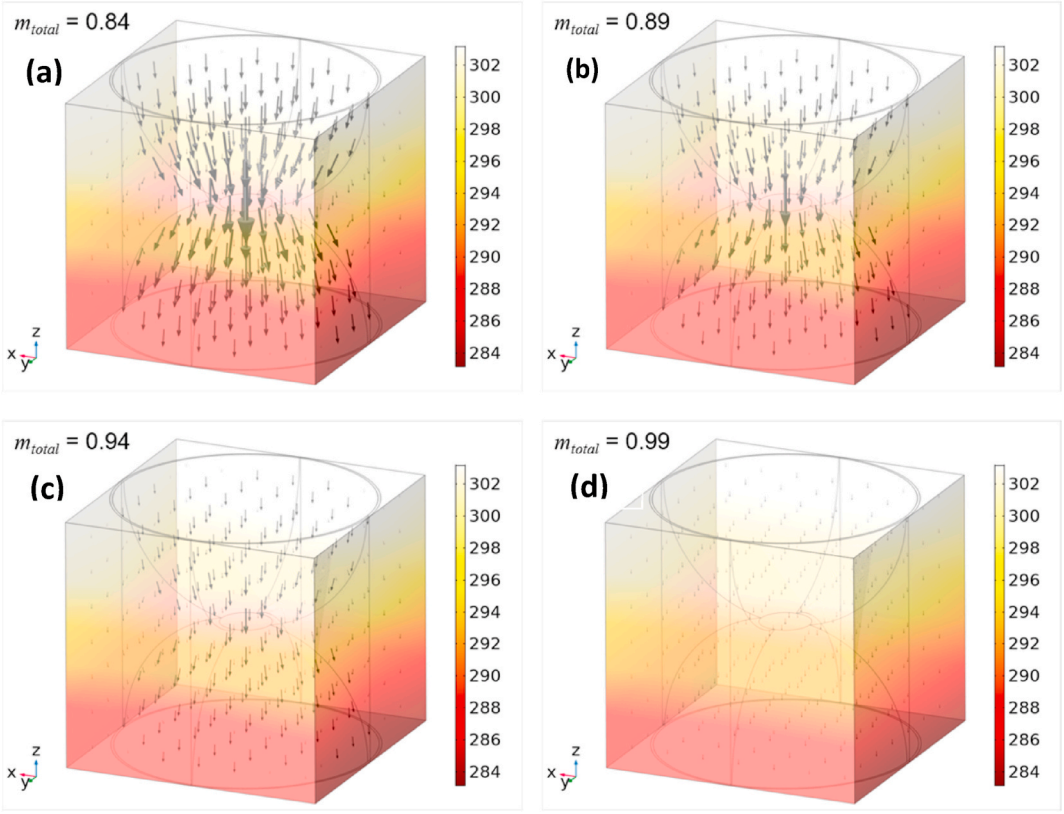

Fig. 11. Temperature distribution inside a simple cubic geometry with different values of total porosity, m_{total} (a = 0.84, b = 0.89, c = 0.94 and d = 0.99). Black arrows represent the conductive heat flux. The temperature bar shows the temperatures in Kelvin.

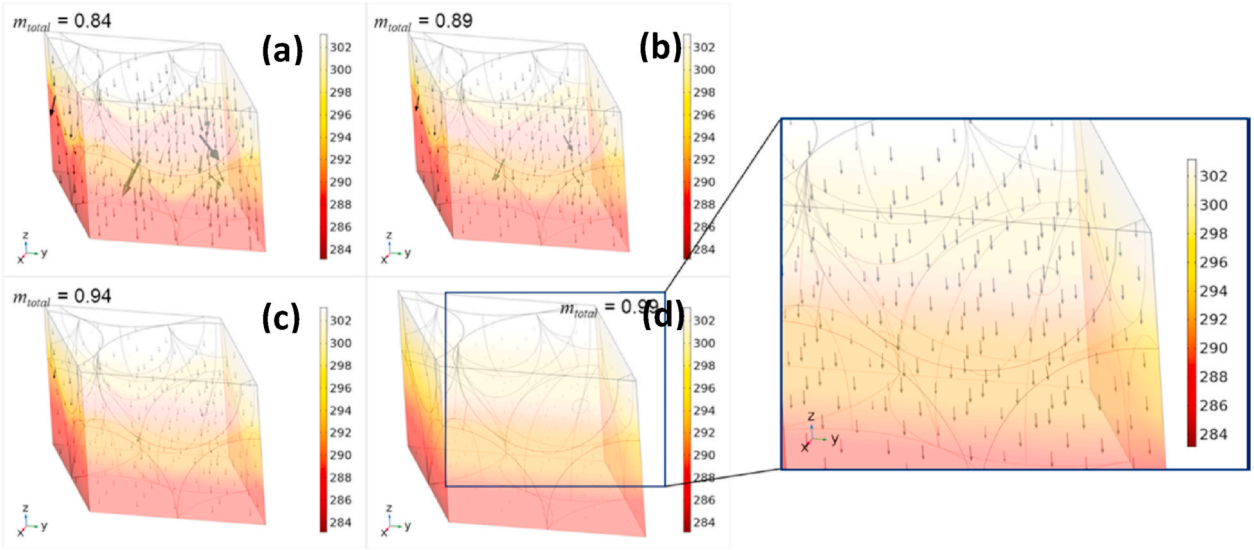

Fig. 12. Temperature distribution inside a hexagonal geometry with different values of particle porosity, m_{total} (a = 0.84, b = 0.89, c = 0.94 and d = 0.99). Black arrows represent the conductive heat flux. The temperature bar shows the temperatures in Kelvin.

2.2.2. Governing equations in domain elements

The conduction heat transfer in the domain elements was calculated by the steady state heat transfer equation (equation (5)) and the three-dimensional Fourier's law (equation (6)). The total heat flux, calculated at the lower face of the unit cell, was used to derive the thermal conductivity of the unit cell (k_c) using Fourier's law on the whole unit cell (equation (7)).

$$\frac{\partial}{\partial x}\left(k_i\frac{\partial T}{\partial x}\right)+\frac{\partial}{\partial y}\left(k_i\frac{\partial T}{\partial y}\right)+\frac{\partial}{\partial z}\left(k_i\frac{\partial T}{\partial z}\right)=0 \tag{5}$$

$$\dot{Q_{c,w}}=-k_iA\frac{\partial T}{\partial w} \tag{6}$$

$$k_c=-\dot{Q_u}\frac{l_u}{A_u\Delta T_u} \tag{7}$$

where k_i is either the thermal conductivity of the grain (k_{gr}) or the gas inside pore (k_g), based on the mesh element, T the temperature, $\dot{Q_{c,w}}$ the rate of heat conduction at a point on an isothermal surface whose normal is given by the vector w, A the area of surface normal to the direction of heat flux, k_c the conductive thermal conductivity of unit cell, Q_u the heat flux calculated at one of the faces of the unit cells, l_u the length of the unit cell, A_u the area of top/bottom surface of the unit cell and ΔT_u the temperature difference between the two surfaces i.e. 20 °C.

2.2.3. Grain's thermal conductivity

In both the packings, grain's or particle's thermal conductivity (k_{gr}) is a common input parameter. For a porous object, irrespective of its shape, or the shape of the pores, the thermal conductivity can be calculated using Russel's equation (equation (8)), which depends on the porosity of the object, the gaseous conductivity in the pores and the

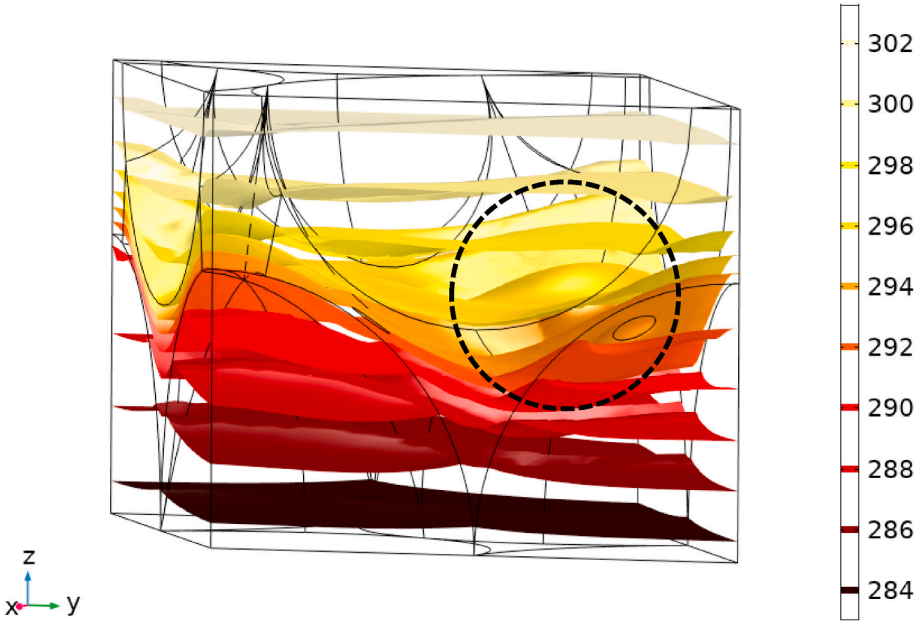

Fig. 13. Isothermal contours inside a hexagonal geometry, with total porosity = 0.89. The contours are highly non-linear and are bulged near the contact areas, shown with dashed circle. The temperature bar shows the temperatures in Kelvin.

Table 2
Parameters used in simulations and their value while constant or being varied.

Parameter	Value (constant)	Value (range)
D	100 μm	50–500 μm
D_{pp}	5 μm	1–100 μm
m	0.95	–
m_{total}	0.974 (SC), 0.963 (Hex)	0.80–0.98
p	0.1 mbar	0.001–1000 mbar
a/D	0.1	0.01–0.65
k_T	1 $Wm^{-1}K^{-1}$	–

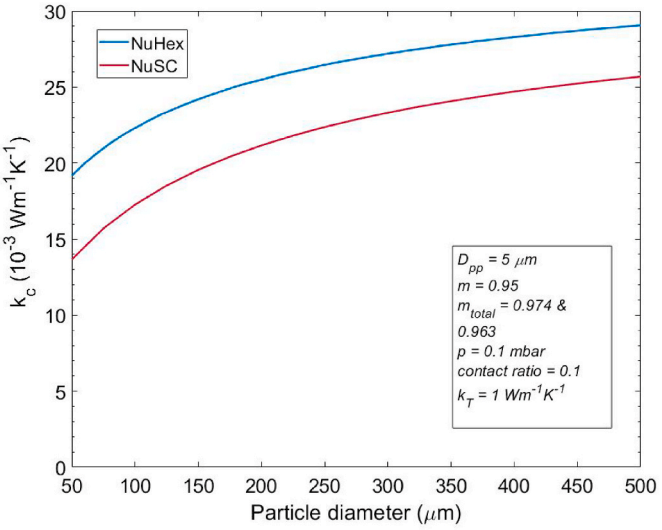

Fig. 14. Effect of particle size on total thermal conductivity for different packings.

thermal conductivity of the bulk material [36]. The gaseous conductivity in the pores further depends on the intra-particle pore size and the evacuation pressure (equation (2)).

$$k_{gr} = k_T \times \left(\frac{m^{2/3} + \nu\left(1 - m^{2/3}\right)}{m^{2/3} - m + \nu\left(1 - m^{2/3} + m\right)} \right) \tag{8}$$

where k_T is the thermal conductivity of the bulk material (SiO_2 in case of perlite), m the porosity of the grain, ν the ratio of k_T and k_g, and k_g the gaseous conductivity of the intra-particle pore, which can be calculated using equation (2).

Measurement of the porosity of the grain is a difficult process requiring extensive measurement techniques and instrumentation. However, it is known that perlite particles expand 15–20 times when heated rapidly. Thus, a reasonable guess of perlite grain's porosity can be made using equation (9).

$$m = \frac{(x-1) + \phi_i}{x} \tag{9}$$

where x is multiplication factor of increase in particle's volume and ϕ_i the initial porosity of the perlite particle.

Using x as 19 and ϕ_i as 0.05, one gets a value of 0.95 for grain's porosity.

2.3. Results from the conduction models

Figs. 11–13 show the temperature distribution and heat flux inside the simple cubic and hexagonal geometries. The temperature varies from 30 °C at the top face to 10 °C at the bottom. The black arrows represent the conductive heat flux, with their size being proportional to the magnitude of the heat flux. The bended arrows near the contact

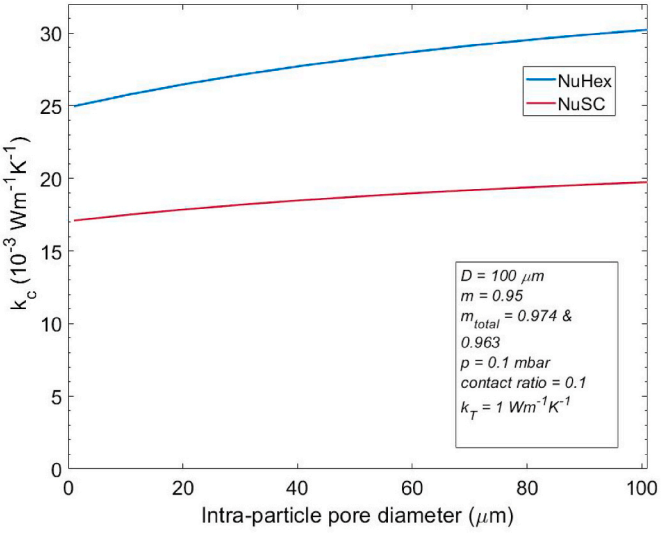

Fig. 15. Effect of intra-particle pore size on total thermal conductivity for different packings.

point in Figs. 11a and 12a shows that the majority of the heat travels through the particles when the particle porosity is low, whereas as the porosity increases, the bending of the heat flux towards the particle-particle contact decreases. The results are in line with expected results discussed above (Fig. 5). The isothermal contours in the hexagonal geometry have been presented in Fig. 13. The contours are highly non-linear and bulged near the contact area of the particles.

The conductive heat transfer model, to calculate k_c, was run while varying five parameters – i) particle diameter (D), ii) intra-particle pore diameter (D_{pp}), iii) total porosity (m), iv) internal gas pressure (p) and v) contact ratio (a/D) for simple cubic and hexagonal packing arrangements (Table 2). The results are shown in Fig. 14 – Fig. 18. The results from the simple cubic model have been referred as NuSC (Numerical Simple Cubic) and those from hexagonal model as NuHex (Numerical Hexagonal). It is important to note that these results don't include the effect of radiation. Particle size, intra-particle pore size and total porosity are material properties and can be altered while manufacturing the perlite. The temperature and the rate at which volcanic glass is heated produce different particle size, intra-particle pore size and particle's porosity. Inter-particle pore size and packing porosity can be altered by efficient filling and compaction methods. Internal gas pressure and contact ratio are controlled while designing the insulation.

The knowledge of the effects of these parameters on the thermal conductivity can lead to a design framework to produce energy-efficient and cost-efficient insulation. The model though demonstrated for perlite can be used for any type of porous insulation with spherical particles, such as glass micro-beads. A pointwise discussion on the results from the model is presented here.

1. Thermal conductivity, in both packings, increased weakly with increasing particle size (Fig. 14). Whereas particle size itself doesn't affect the thermal conductivity, but increasing particle size leads to an increase in the inter-particle pore size and thus the gaseous conduction following the Knudsen effect as described in equation (2). The thermal conductivity increased by 1.5–1.8 times when particle size increased from 50 μm to 500 μm. The trend of this increase was similar to that observed by Sakatani et al. [37] while measuring the solid conductivity of soda-lime glass beads. It is noteworthy that Fig. 14 was plotted for an evacuation pressure of 0.1 mbar and the magnitude is expected to be more prominent at higher pressures. Particle size affects the wave scattering and absorption behaviour of the powder and thus the radiative conductivity. In physical terms, particle size determines density of materials. Keeping all other

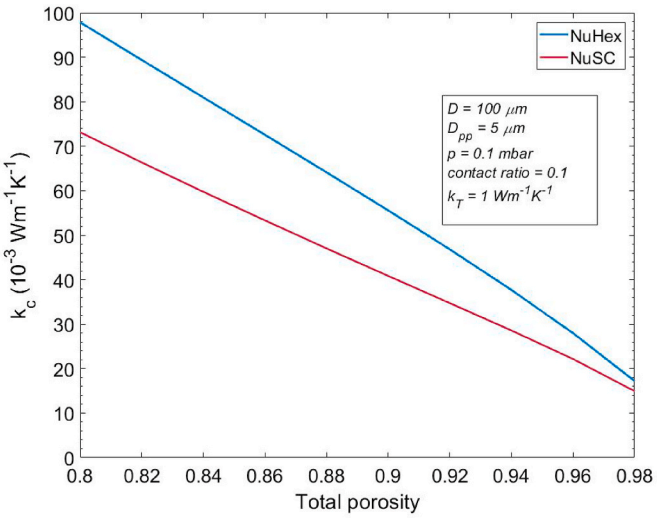

Fig. 16. Effect of porosity on total thermal conductivity for different packings.

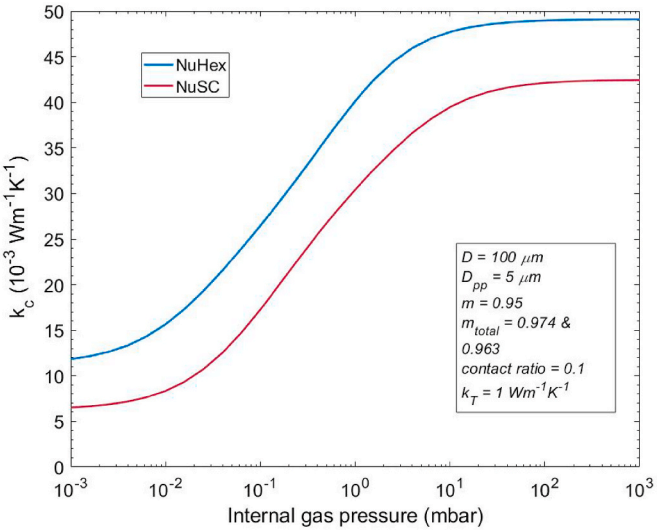

Fig. 17. Effect of internal gas pressure on total thermal conductivity for different packings.

factors same, an insulation made with a smaller particle size material would be heavier than that made with bigger particles of the same material. Additionally, particle size also impacts flow of powder, cohesiveness among particles and compressibility [38].

2. The intra-particle pore size showed a weak effect on the thermal conductivity of porous insulation at low pressures (Fig. 15). The thermal conductivity increased by 1.1–1.2 times when intra-particle pore size increased from 1 μm to 100 μm. Shorter intra-particle pore size restricts gaseous conduction reducing the grain's thermal conductivity (equation (8)) and thus the overall thermal conductivity. Here, it was assumed that the change in intra-particle pore size is independent of the porosity of the particle.
3. The overall porosity had a significant effect on the thermal conductivity. While plotting Fig. 16, the inter-particle porosity, which depends on the type of packing, was kept constant (0.476 for simple cubic and 0.26 for hexagonal packing) and the variation in total porosity was due to change in the on-particle porosity.

   As the porosity of the particle decreased, grains became more conductive due to increase in the bulk material mass (equation (8)). This led to high heat flux transferred through the grains. The effect was more prominent in the case of hexagonal packing as compared to simple cubic because of a higher number of particles per unit volume (Figs. 4 and 8). A similar trend was observed by Sakatani et al. [37] for low-alkali glass beads. As shown in Fig. 5, the effect of porosity on thermal conductivity could not be fully accounted for by an analytical solution considering various series or parallel heat transfer paths because it neglects heat transfer within the particle at the particle-gas boundary.

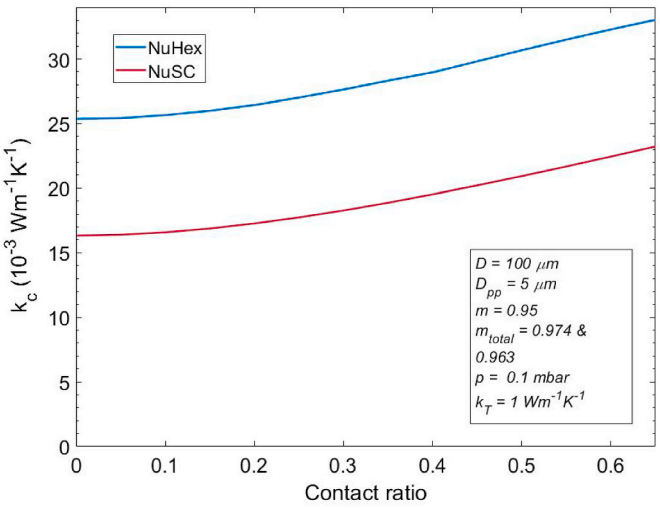

Fig. 18. Effect of contact area among particles on total thermal conductivity for different packings.

4. The effect of internal gas pressure on thermal conductivity is a characteristic curve for any vacuum insulation core material. A change in internal gas pressure causes change in the thermal conductivity of the pore space due to increased mean free path length of the gas in it (equation (2)). Since, the size of all pores (inter and intra-particle) is different, the effect of change in pressure is different for all pores. The thermal conductivity thus becomes a complex function of internal gas pressure (Fig. 17). The results obtained are similar to those measured by Beikircher et al. [17] for expanded perlites.

   The effect of change in internal gas pressure in intra-particle pores directly affects the grain's thermal conductivity (equation (8)), while the same change in the inter-particle pores affects the respective pore's conductivity independently. This effect has been represented in other models in literature as the superimposition of two independent contributions to gaseous conductivity because of two types of pores [39] or by two $p_{1/2}$ values, one for inter-particle pores and the other for intra-particle pores [12,34].

   One interesting aspect of the present model is that it automatically considered the effect of interaction or coupling between grains and the gas. The term coupling conductivity is often used to denote the rise in thermal conductivity when the pores bounded by grain walls act as a thermal bridge for the heat to transport. A separate computation of coupling must be done in decoupled models where the paths of heat transferring through solid and gas are assumed to be parallel, as it becomes a significant heat transfer path at higher pressures (>10 mbar).

   The formulation to compute coupling conductivity has been published for different materials like aerogels [15,18,40] and perlite [17] besides having been experimentally measured [41,42]. However, a general formula for computation of coupling is not available. The present model shows that a part of this coupling heat transfer occurs due to the inter-particle pores partially bounded by walls of grains, such as the cross-wise pores in simple cubic geometry and the tetrahedral pores in hexagonal geometry. The other part of this coupling arises due to intra-particle pores. This also answers the question on why *'coupling'* doesn't occur in foams – they don't have bounded inter-particle or intra-particle pores.

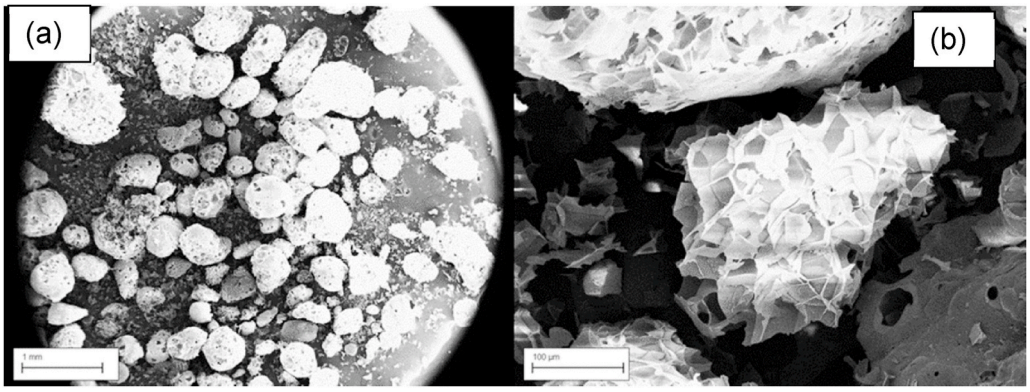

Fig. 19. SEM images of the expanded perlite at different magnifications: a) 30× and b)500× with a 10 keV electron beam.

5. The contact ratio between the particles is yet another important factor which affects the thermal conductivity (Fig. 18). There are two methods of changing the density of a powder bed. One of them is change in packing order, also known as grain rearrangement, which can be achieved by efficient filling of insulation in the cavity/envelope. The other is application of external pressure on the powder bed. Application of external pressure or compaction leads to a) grain rearrangement, b) grain deformation and c) pressure solution, i.e. dissolution of the particle due to excessive stress [31]. Packing of grains remaining constant and pressure solution/particle dissolution neglected, one can assume that application of external pressure mainly causes grain deformation, thereby increasing the contact ratio between them. Thus, the contact ratio is a representation of external pressure on the powder bed, or the density.
   As the contact ratio increased, the heat flux leakage through the grains increased, increasing the total thermal conductivity. The effect was more prominent in hexagonal packing because there were more contacts per unit volume of hexagonal packing as compared to simple cubic packing. It was noteworthy that this effect was only prominent at lower internal gas pressures when the grain's thermal conductivity was much higher than the thermal conductivity of the gas in pores. The contact ratio in the present research also includes the effect of the contact resistance.

3. Experimental validation

This section presents the experimentally measured total thermal conductivity of a perlite-core vacuum insulation panel developed during the study. Commercially available expanded perlite was procured and detailed lab tests were performed to determine particle size distribution, pore size distribution and particle morphology. The results of these material characterization tests were used as input parameters in the model described in section 2 to predict the thermal conductivity of the panels. VIP panels were manufactured using this perlite by first compressing the powder to a desired density and thickness, and then sealing these perlite boards in a metallized laminate at the desired internal gas pressure. The total thermal conductivity of the panel was measured at internal gas pressures ranging from 0.1 mbar to 500 mbar, an uncertainty analysis was performed and the results compared with those predicted by the model.

3.1. Material characterisation

The following lab tests were performed to measure material properties of the expanded perlite both qualitatively and quantitatively. The material properties include particle shape, size, morphology, distribution, pore size and porosity.

i) Scanning Electron Microscopy (SEM)

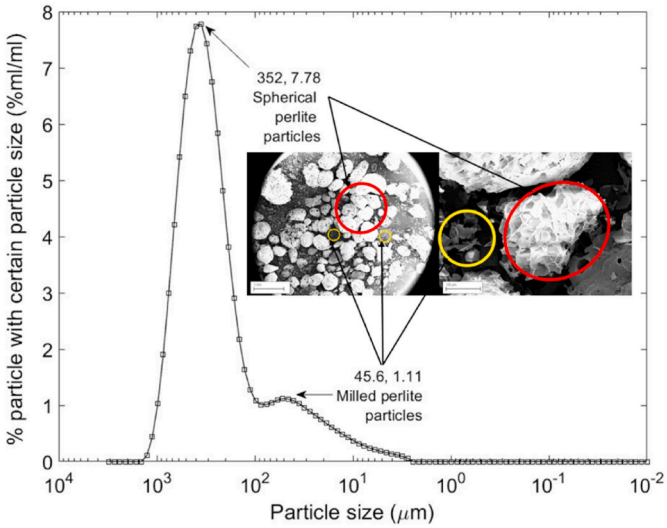

Fig. 20. Particle size distribution of an expanded perlite obtained by laser diffraction.

The perlite was observed under an SEM (LEO 1455VP) to observe the shapes, distribution and morphology of the particles and sizes of particles. As shown in Fig. 19, the perlite consisted of two types of particles - a) big porous spherical particles, which have open intra-particle pores,

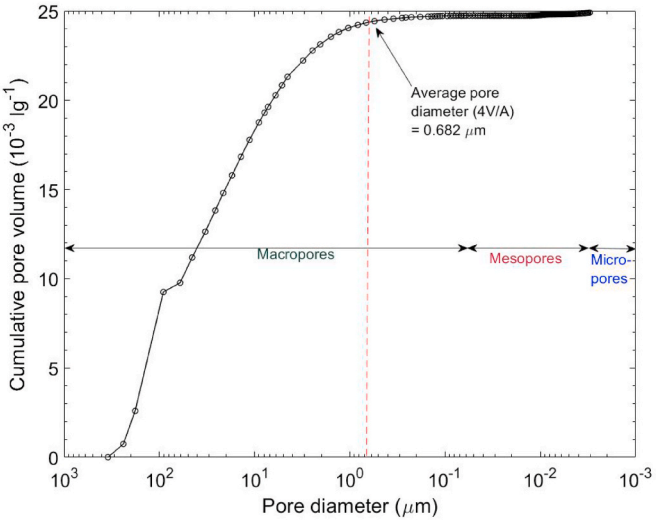

Fig. 21. Cumulative intrusion pore size distribution of the perlite.

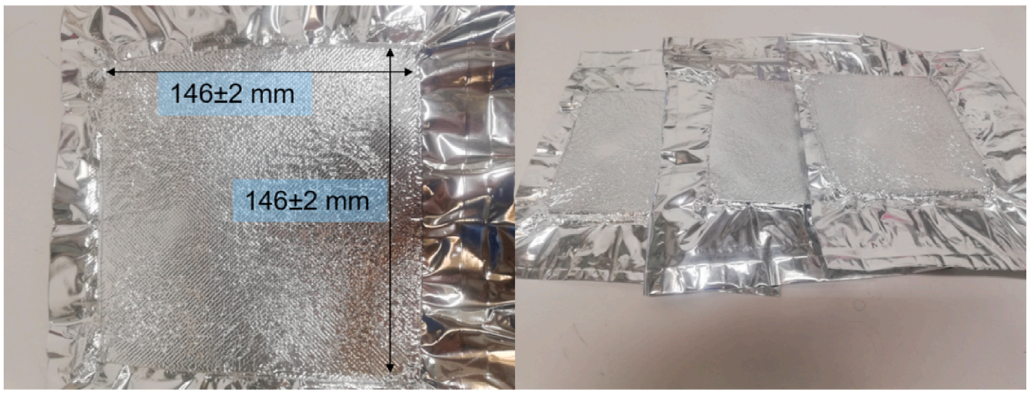

Fig. 22. Vacuum insulation panel samples manufactured in this research.

Table 3
Properties of VIPs developed and tested.

Sample	Side length (mm)	Thickness (mm)	Density (kgm^{-3})	k_r (10^{-3} $Wm^{-1}K^{-1}$)
A	146	11.38	172.4	1.43
B	146	14.59	134.5	1.83
C	146	14.48	135.5	1.82

and b) small flake shaped particles, which is milled perlite.

ii) Laser Diffraction

The distribution of particle sizes was determined by laser diffraction-based particle size analyser (Fig. 20). The results showed two peaks, which could be attributed to big spherical particles (352 μm) and small milled particles (45.6 μm), as were observed under SEM. The proportion of milled particles was much lower than the big particles. Since, the developed model has been developed for mono-sized particles, a single representative particle diameter was defined as the weighted average of particle diameters of the two peaks, which in the present case was $\left(\frac{352\times7.78 + 45.6\times1.11}{7.78+1.11}\right)\mu m = 313.74\,\mu m$.

iii) Mercury Intrusion Porosimetry (MIP)

The distribution of pore sizes and the overall porosity of the perlite was determined by MIP measurements (Autopore IV). A wide range of pore sizes ranging from 0.003 μm to 300 μm were observed, shown in Fig. 21. The average pore size, which represents the representative pore size of the sample could be calculated as 4V/A, where V is the total intrusion volume in the sample and A the total surface area of the pores. The average pore size was calculated to be 0.682 μm. For a mono particle size powder bed, the particle size of 313 μm must represent much higher pore size. However, the migration of milled particles into the pores of spherical perlite particles give rise to much lower pore size, of the order of 0.1 μm. The overall porosity was measured to be 97.92%. The results obtained using MIP are for loose perlite, with density of 39.3 kg/m^3. The pore size and the porosity, both reduce when the density is increased due to compression, and could be calculated using equations (10) and (11).

$$D_p = \frac{4}{S}\left(\frac{1}{\rho} - \frac{1}{\rho_s}\right) \tag{10}$$

$$m_{total} = 1 - \frac{\rho}{\rho_s} \tag{11}$$

where D_p is the size of the pore, S the surface area of the pore, ρ the density of the powder, ρ_s the skeletal density of the powder and m_{total} the porosity of the powder.

Fig. 23. Heat flow meter (HFM 446 lambda) used to measure the thermal conductivity of the VIP samples.

3.2. Thermal conductivity measurement

Three vacuum insulation panels (A, B and C) were prepared using perlite as the core material and sealed in a metallized laminate (Fig. 22), as detailed in Table 3. While samples B and C were similar to each other in terms of density and thickness, sample A's density was made higher by compressing the core to a lower thickness. The thermal conductivity of these VIPs was measured at different evacuation pressures between 0.1 mbar and 500 mbar using a calibrated heat flow meter (Figs. 23 and 24). The HFM was calibrated as per ASTM C1667 – 15 [43] which details the test method for using heat flow meter apparatus to measure the center-of-panel thermal transmission properties of vacuum insulation panels. After completion of each test, the VIP's core pressure was measured using a laser-based technique involving the foil lift off method [44].

The heat flow meter measures total thermal conductivity, which includes the effect of the heat transfer by radiation. This effect of radiation was removed to enable comparison between measured and modelled thermal conductivity. As perlites are optically thick mediums, the conductive and radiative heat exchanges through them can be superimposed. The radiative conductivity of perlite could be calculated using the diffusion equation (equation (12)) [3,12,45,46].

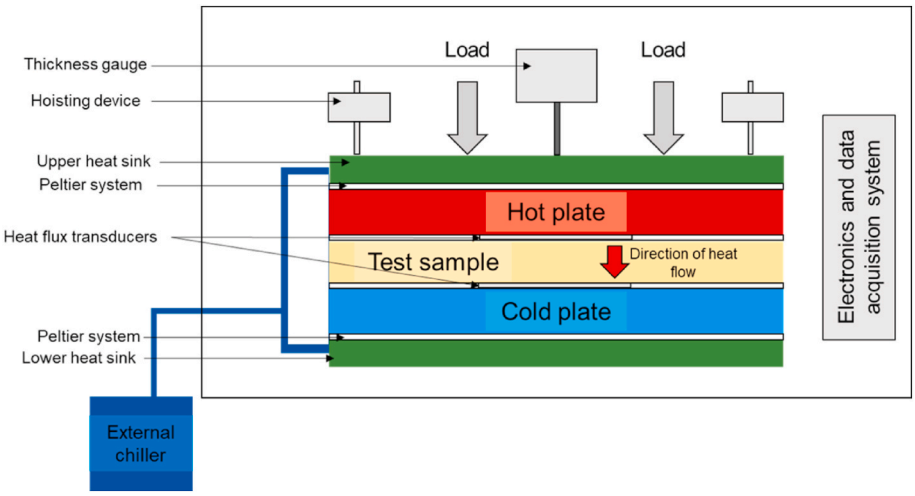

Fig. 24. Schema of an HFM 446 lambda.

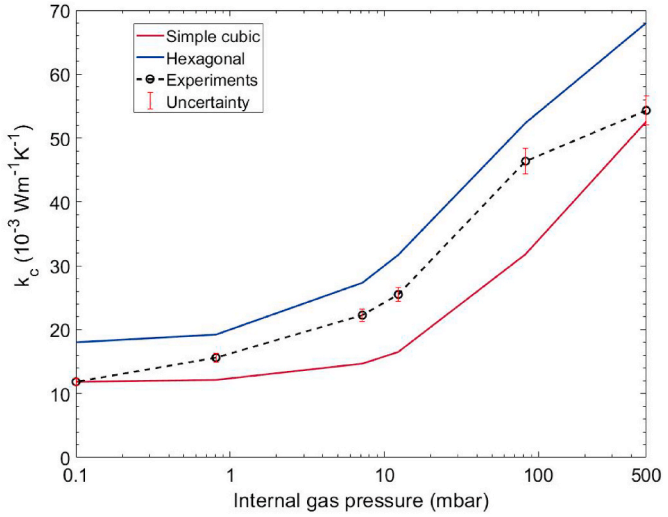

Fig. 25. Comparison of measured results with the modelling bounds for sample A.

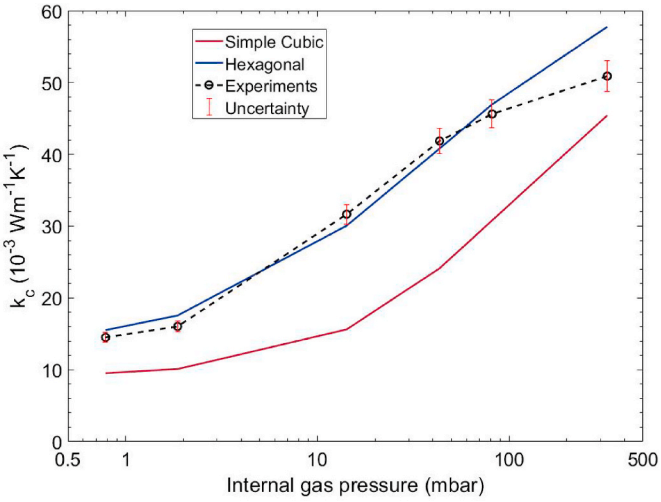

Fig. 26. Comparison of measured results with the modelling bounds for sample B.

$$k_r = \frac{16n^2\sigma T^3}{3\rho e} \tag{12}$$

$$k_{VIP,measured} = k_c + k_r = k_c + \frac{16n^2\sigma T^3}{3\rho e} \tag{13}$$

$$k_c = k_{VIP,measured} - \frac{16n^2\sigma T^3}{3\rho e} \tag{14}$$

where k_r is the radiative conductivity, n the real part of the refractive index, σ the Stefan-Boltzmann constant, T the mean operating temperature, ρ the density of the material, e the specific extinction coefficient, $k_{VIP,\ measured}$ is the total thermal conductivity of the VIP measured using heat flow meter, k_c the conductive thermal conductivity.

The refractive index of the expanded perlite was taken to be 1.05 owing to its high porosity (98%) and the specific extinction coefficient, e, which is required to calculate the radiative conductivity of the perlite in equation (12), was taken from literature as 38 ± 4 m^2/kg [17]. The calculated radiative conductivity at 20 °C has been given in Table 3.

The uncertainty involved in the thermal conductivity measurements are due to a range of factors including measurements of VIPs' dimensions, test temperature and the rate of heat flux. The individual uncertainties in the calculation of k_{VIP} and k_r were calculated using law

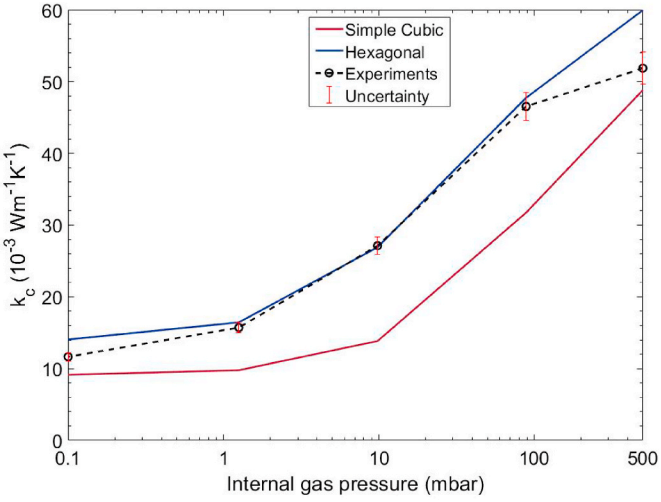

Fig. 27. Comparison of measured results with the modelling bounds for sample C.

Table 4
Parameters used for comparison between experiments and modelling.

Parameter	Value (constant)	
D	313.7 μm	Representative particle diameter
D_p	0.15 μm (Sample A) or 0.19 μm (Sample B, C)	Representative pore diameter for all pores
m_{total}	0.91 (Sample A), 0.93 (Sample B, C)	Total porosity
a/D	0.1	Contact ratio
k_T	1 $Wm^{-1}K^{-1}$	Base thermal conductivity

of propagation of errors (equation (15)) and the total uncertainty in k_c was calculated using equation (16).

$$uncertainty = \sqrt{\sum \left(\frac{\partial \ln f}{\partial x_i}\right)^2 (\delta x_i)^2} = \sqrt{\sum \left(\frac{\delta x_i}{x_i}\right)^2} \quad (15)$$

$$\delta k_c = \sqrt{\left(\delta k_{VIP,measured}\right)^2 + \left(\delta k_r\right)^2} \quad (16)$$

where f is the function to calculate thermal conductivity (Fourier's law), x_i the independent variables on which the thermal conductivity depends and δx_i the uncertainty associated with measurements of these independent variables. The total calculated uncertainty in k_c ranged from $\pm 0.55 \times 10^{-3}$ $Wm^{-1}K^{-1}$ at 0.1 mbar to $\pm 2.27 \times 10^{-3}$ $Wm^{-1}K^{-1}$ at 500 mbar.

3.3. Comparison with model

Predicted and measured thermal conductivity for the three VIPs investigated are presented in Figs. 25–27. The inputs to the prediction model were given based on the material characterisation performed on the perlite powder, see Table 4. The contact ratio was taken to be 0.1, since there was no direct way to measure it. As can be observed, the measured conductivity values of sample A lied well within the bounds described by the model. Samples B and C's measured values were closer to hexagonal model as compared to the simple cubic model.

4. Conclusions

A theoretical framework to predict the thermal conductivity of expanded perlite was developed and experimentally validated. Due to the random packing structure of powders, the thermal conductivity related to the conductive heat transfer via the solid and gaseous phase couldn't be extracted. However, the upper and lower bounds of this conductive heat transfer were calculated as the thermal conductivities of simple cubic and hexagonal packing structures respectively. Due to complex geometries involved, the thermal conductivity of particle beds arranged in these two packing structures was numerically calculated using finite element method. Using the parameters mentioned in Table 2, it was observed that the thermal conductivity increased by 1.5–1.8 times when particle size increased from 50 μm to 500 μm, 1.1–1.2 times when intra-particle pore size increased from 1 μm to 100 μm, 5–6 times when porosity of the bed decreased from 0.98 to 0.8, 4–6 times when pressure increased from 0.001 mbar to 1000 mbar.

A grade of expanded perlite was procured from and tested for its particles' shape, size, morphology, pore size, porosity. It was observed that the perlite also comprised of a small proportion of milled particles in addition to the large spherical shaped porous particles. The average particle size was calculated to be 313 μm. The average pore diameter was measured to be 0.682 μm and the porosity to be 97.92%. The conductive thermal conductivity was calculated from the model using these parameters. Three vacuum insulation panels were manufactured using this perlite and their thermal conductivity was tested at different pressures in the range of 0.1 mbar–500 mbar. The effect of radiation was subtracted from the measured results in order to compare them with the predicted conductive thermal conductivity. The total thermal conductivity of expanded perlite based vacuum insulation panels manufactured in lab lied well between bounds defined by the model developed.

Declaration of competing interest

The authors declare that they have no known competing financial interests or personal relationships that could have appeared to influence the work reported in this paper.

Data availability

Data will be made available on request.

References

[1] M. Alam, H. Singh, S. Suresh, D.A.G. Redpath, Energy and economic analysis of Vacuum Insulation Panels (VIPs) used in non-domestic buildings, Appl. Energy 188 (2017) 1–8, https://doi.org/10.1016/j.apenergy.2016.11.115.
[2] F.A. Almeida, J. Corker, N. Ferreira, M.A. Neto, M. Fan, H. Beyrichen, R. Caps, Alternative low cost based core systems for vacuum insulation panels, Ciência Tecnol. Dos Mater. 29 (2017) 151–156, https://doi.org/10.1016/j.ctmat.2016.10.002.
[3] M. Alam, H. Singh, S. Brunner, C. Naziris, Experimental characterisation and evaluation of the thermo-physical properties of expanded perlite - fumed silica composite for effective vacuum insulation panel (VIP) core, Energy Build. 69 (2014) 442–450, https://doi.org/10.1016/j.enbuild.2013.11.027.
[4] B. Chang, L. Zhong, M. Akinc, Low cost composites for vacuum insulation core material, Vacuum 131 (2016) 120–126, https://doi.org/10.1016/j.vacuum.2016.05.027.
[5] C. Li, B. Li, N. Pan, Z. Chen, M.U. Saeed, T. Xu, Y. Yang, Thermo-physical properties of polyester fiber reinforced fumed silica/hollow glass microsphere composite core and resulted vacuum insulation panel, Energy Build. 125 (2016) 298–309, https://doi.org/10.1016/j.enbuild.2016.05.013.
[6] C.D. Li, M.U. Saeed, N. Pan, Z.F. Chen, T.Z. Xu, Fabrication and characterization of low-cost and green vacuum insulation panels with fumed silica/rice husk ash hybrid core material, Mater. Des. 107 (2016) 440–449, https://doi.org/10.1016/j.matdes.2016.06.071.
[7] J. Zhuang, S.H. Ghaffar, M. Fan, J. Corker, Restructure of expanded cork with fumed silica as novel core materials for vacuum insulation panels, Compos. B Eng. 127 (2017) 215–221, https://doi.org/10.1016/j.compositesb.2017.06.019.
[8] V. Nemanič, M. Žumer, New organic fiber-based core material for vacuum thermal insulation, Energy Build. 90 (2015) 137–141, https://doi.org/10.1016/j.enbuild.2015.01.012.
[9] Z. Chen, Z. Chen, Z. Yang, J. Hu, Y. Yang, L. Chang, L.J. Lee, T. Xu, Preparation and characterization of vacuum insulation panels with super-stratified glass fiber core material, Energy 93 (2015) 945–954, https://doi.org/10.1016/j.energy.2015.08.105.
[10] S. Verma, H. Singh, Vacuum insulation panels for refrigerators, Int. J. Refrig. 112 (2020) 215–228, https://doi.org/10.1016/j.ijrefrig.2019.12.007.
[11] G.H. Tang, C. Bi, Y. Zhao, W.Q. Tao, Thermal transport in nano-porous insulation of aerogel: factors, models and outlook, Energy 90 (2015) 701–721, https://doi.org/10.1016/j.energy.2015.07.109.
[12] R. Caps, J. Fricke, Thermal conductivity of opacified powder filler materials for vacuum insulations, Int. J. Thermophys. 21 (2000) 445–452, https://doi.org/10.1023/A:1006691731253.
[13] J. Kim, J.H. Lee, T.H. Song, Vacuum insulation properties of phenolic foam, Int. J. Heat Mass Tran. 55 (2012) 5343–5349, https://doi.org/10.1016/j.ijheatmasstransfer.2012.05.051.
[14] J.S. Kwon, C.H. Jang, H. Jung, T.H. Song, Effective thermal conductivity of various filling materials for vacuum insulation panels, Int. J. Heat Mass Tran. 52 (2009) 5525–5532, https://doi.org/10.1016/j.ijheatmasstransfer.2009.06.029.
[15] C. Bi, G.H. Tang, Z.J. Hu, H.L. Yang, J.N. Li, International Journal of Heat and Mass Transfer Coupling model for heat transfer between solid and gas phases in aerogel and experimental investigation 79 (2014) 126–136, https://doi.org/10.1016/j.ijheatmasstransfer.2014.07.098.
[16] J. Fricke, H. Schwab, U. Heinemann, Vacuum insulation panels–exciting thermal properties and most challenging applications, Int. J. Thermophys. 27 (4) (2006 Jul 1) 1123–1139.
[17] T. Beikircher, M. Demharter, Heat transport in evacuated perlite powders for super-insulated long-term storages up to 300 °C, J. Heat Tran. 135 (2013), 051301, https://doi.org/10.1115/1.4023351.
[18] J.J. Zhao, Y.Y. Duan, X.D. Wang, B.X. Wang, Effects of solid–gas coupling and pore and particle microstructures on the effective gaseous thermal conductivity in aerogels, J. Nanoparticle Res. 14 (8) (2012 Aug) 1–5.
[19] M. Alam, Development of Vacuum Insulation Panel with Low Cost Core Material, PhD Thesis, Brunel University London, 2015. https://bura.brunel.ac.uk/bitstream/2438/11658/1/FulltextThesis.pdf.
[20] S.Q. Zeng, A. Hunt, R. Greif, Geometric structure and thermal conductivity of porous medium silica aerogel, J. Heat Tran. 117 (1995) 1055–1058, https://doi.org/10.1115/1.2836281.

[21] G. Lu, X. Wang, Y. Duan, X. Li, Effects of Non-ideal Structures and High Temperatures on the Insulation Properties of Aerogel-Based Composite Materials, vol. 357, 2011, pp. 3822–3829, https://doi.org/10.1016/j.jnoncrysol.2011.07.022.
[22] G. Wei, Y. Liu, X. Zhang, F. Yu, X. Du, Thermal conductivities study on silica aerogel and its composite insulation materials, Int. J. Heat Mass Tran. 54 (2011) 2355–2366, https://doi.org/10.1016/j.ijheatmasstransfer.2011.02.026.
[23] G. Wei, Y. Zhang, C. Xu, X. Du, Y. Yang, A thermal conductivity study of double-pore distributed powdered silica aerogels, Int. J. Heat Mass Tran. 108 (2017) 1297–1304, https://doi.org/10.1016/j.ijheatmasstransfer.2016.12.062.
[24] C. Bi, G.H. Tang, Z.J. Hu, Heat conduction modeling in 3-D ordered structures for prediction of aerogel thermal conductivity, Int. J. Heat Mass Tran. 73 (2014) 103–109, https://doi.org/10.1016/j.ijheatmasstransfer.2014.01.058.
[25] J. Fricke, R. Caps, Heat transfer in thermal insulations-Recent progress in analysis, Int. J. Thermophys. 9 (1988) 885–895, https://doi.org/10.1007/BF00503253.
[26] K.K. Chatterjee, Uses of Industrial Minerals, Rocks and Freshwater, Nova Science Publishers, 2009. http://dl.merc.ac.ir/handle/Hannan/19988.
[27] J. Bernal, J. Mason, Packing of spheres: co-ordination of randomly packed spheres, Nature 188 (1960) 910–911.
[28] G.D. Scott, Packing of spheres: packing of equal spheres, Nature 188 (1960) 908–909.
[29] G.D. Scott, Radial distribution of the random close packing of equal spheres, Nature 194 (1962) 956–957.
[30] G. Nolan, P. Kavanagh, Computer simulation of random packing of hard spheres, Powder Technol. 72 (1992) 149–155.
[31] L.J.H. Alberts, Initial Porosity of Random Packing: Computer Simulation of Grain Rearrangement, Delft University of Technology, 2005. https://repository.tudelft.nl/islandora/object/uuid:fa3b8d33-3eda-474a-bebd-87f43dd58873/datastream/OBJ.
[32] G.Y. Onoda, E.G. Liniger, Random loose packings of uniform spheres and the dilatancy onset, Phys. Rev. Lett. 64 (1990), https://doi.org/10.1103/PhysRevLett.64.2727.
[33] J. Finney, Random packings and the structure of simple liquids. I. The geometry of random close packing, in: Proc. R. Soc. London. A. Math. Phys. Sci., The Royal Society London, 1970, pp. 479–493.
[34] M. Kaganer, Thermal Insulation in Cryogenic Engineering, 1969.
[35] E.J.F. Dickinson, H. Ekström, E. Fontes, COMSOL Multiphysics®: finite element software for electrochemical analysis. A mini-review, Electrochem. Commun. 40 (2014) 71–74, https://doi.org/10.1016/j.elecom.2013.12.020.
[36] H. Russell, Principles of heat flow in porous insulators, J. Am. Ceram. Soc. 18 (1935) 1–5.
[37] N. Sakatani, K. Ogawa, Y. Iijima, M. Arakawa, R. Honda, S. Tanaka, Thermal conductivity model for powdered materials under vacuum based on experimental studies, AIP Adv. 7 (2017), https://doi.org/10.1063/1.4975153.
[38] A. Hart, Effect of particle size on detergent powders flowability and tabletability, J. Chem. Eng. Process Technol. 6 (2015). https://www.longdom.org/open-access/effect-of-particle-size-on-detergent-powders-flowability-and-tabletability-2157-7048.1000215.pdf.
[39] G. Reichenauer, U. Heinemann, H.P. Ebert, Relationship between pore size and the gas pressure dependence of the gaseous thermal conductivity, Colloids Surfaces A Physicochem. Eng. Asp. 300 (2007) 204–210, https://doi.org/10.1016/j.colsurfa.2007.01.020.
[40] K. Swimm, S. Vidi, G. Reichenauer, H. Ebert, Coupling of gaseous and solid thermal conduction in porous solids Solid phase Gas phase Solid phase, J. Non-Cryst. Solids 456 (2017) 114–124, https://doi.org/10.1016/j.jnoncrysol.2016.11.012.
[41] J.J. Zhao, Y.Y. Duan, X.D. Wang, B.X. Wang, Effects of solid-gas coupling and pore and particle microstructures on the effective gaseous thermal conductivity in aerogels, J. Nanoparticle Res. 14 (2012), https://doi.org/10.1007/s11051-012-1024-0.
[42] K. Swimm, G. Reichenauer, S. Vidi, Impact of Thermal Coupling Effects on the Effective Thermal Conductivity of Aerogels, 2017, pp. 466–474, https://doi.org/10.1007/s10971-017-4437-5.
[43] ASTM C1667-15, Standard Test Method for Using Heat Flow Meter Apparatus to Measure the Center-of-Panel Thermal Transmission Properties of Vacuum Insulation Panels, ASTM International, West Conshohocken, PA, 2015. www.astm.org.
[44] E. Pons, B. Yrieix, S. Brunner, Evaluation of VIPs after mild artificial aging during 10 years: focus on the core behavior, Energy Build. 162 (2018) 198–207, https://doi.org/10.1016/j.enbuild.2017.12.016.
[45] V. Napp, R. Caps, H.P. Ebert, J. Fricke, Optimization of the thermal radiation extinction of silicon carbide in a silica powder matrix, J. Therm. Anal. Calorim. 56 (1999) 77–85, https://doi.org/10.1023/A:1010131324100.
[46] J. Kuhn, S. Korder, M.C. Arduini-Schuster, R. Caps, J. Fricke, Infrared-optical transmission and reflection measurements on loose powders, Rev. Sci. Instrum. 64 (1993) 2523–2530, https://doi.org/10.1063/1.1143914.